Published in final edited form as:

Biomaterials. 2017 November ; 145: 44–55. doi:10.1016/j.biomaterials.2017.08.025.

Multiscale design and synthesis of biomimetic gradient protein/biosilica composites for interfacial tissue engineering

Jin Guo[1,2], **Chunmei Li**[2], **Shengjie Ling**[2,3], **Wenwen Huang**[2], **Ying Chen**[2], and **David L. Kaplan**[*,2]

[1]Department of Chemical and Biological Engineering, Tufts University, 4 Colby Street, Medford, MA 02155, USA

[2]Department of Biomedical Engineering, Tufts University, 4 Colby Street, Medford, MA 02155, USA

[3]Department of Civil and Environmental Engineering, Massachusetts Institute of Technology, Cambridge, MA 02139, USA

Abstract

Continuous gradients present at tissue interfaces such as osteochondral systems, reflect complex tissue functions and involve changes in extracellular matrix compositions, cell types and mechanical properties. New and versatile biomaterial strategies are needed to create suitable biomimetic engineered grafts for interfacial tissue engineering. Silk protein-based composites, coupled with selective peptides with mineralization domains, were utilized to mimic the soft-to-hard transition in osteochondral interfaces. The gradient composites supported tunable mineralization and mechanical properties corresponding to the spatial concentration gradient of the mineralization domains (R5 peptide). The composite system exhibited continuous transitions in terms of composition, structure and mechanical properties, as well as cytocompatibility and biodegradability. The gradient silicified silk/R5 composites promoted and regulated osteogenic differentiation of human mesenchymal stem cells in an osteoinductive environment *in vitro*. The cells differentiated along the composites in a manner consistent with the R5-gradient profile. This novel biomimetic gradient biomaterial design offers a useful approach to meet a broad range of needs in regenerative medicine.

Keywords

Biomimetic; gradient; biomineralization; silk; interface

---

[*]Corresponding author: D.L. Kaplan; david.kaplan@tufts.edu, Fax: 617-627-3231.

Introduction

An attractive feature of natural tissue interfaces is their unique gradient structure [1,2]. Osteochondral interfaces, for example, consist of spatial variation in the extracellular matrix (ECM) composition and orientation from subchondral bone to cartilage [3–5]. Hydroxyapatite (HA) also gradually diminishes from subchondral bone to calcified cartilage and completely disappears in hyaline cartilage [6]. These gradients of minerals and ECM lead to a continuous change of mechanics along the trend [4,7], and also play an important role in connecting mechanically mismatched tissues, facilitating load transmission as well as reducing or eliminating delamination at the junctions [2,4,8,9].

To mimic these natural gradient structures, a variety of biphasic [10–14], multiphasic [15–18], and gradient [4,19–21] composites have been developed. However, unlike natural mineralization during which non-collagenous proteins initiate and regulate mineral formation on the collagenous matrix [22], most of these materials were prepared through mixing inorganic bioactive phase (e.g., chemosynthetic HA crystallites) with additional substrate materials (e.g., collagen) [12,15,18,23–25].

These approaches generally result in weakened structural uniformity and mechanical performance of the resultant composite materials [26,27]. To address these problems, several *in vitro* biomineralization approaches have been reported [9,28] where the nucleation and growth of inorganic mineral phase was regulated directly on well-organized polymer templates. For instance, a three-layer scaffold composed of HA nanocrystals nucleating on self-assembled collagen fibers was developed to support cartilage and bone formation [28]. The gradient mineralization was achieved via changing the ratio of HA/collagen in different layers. However, HA crystallization on self-assembled collagen fibers lacks non-collagenous proteins as mediators of the mineralization process, thus well-controlled mineral deposition on the polymer template is difficult to achieve for the synthesis of advanced materials that mimics the complicated hierarchical natural tissues [29]. Moreover, the use of caustic chemicals during scaffold preparation limits the incorporation of bioactive molecules during material fabrication [9]. Therefore, new strategies are needed to design and synthesize continuous gradient materials using biomimetic mineralization [30].

In this paper, inspired by the growth of natural sponge spicules, we designed a novel route to fabricate gradient protein/biosilica composites via site-specific *in vitro* biomineralization. The biosilica selective peptide-R5, a bioinspired analog derived from the silaffin peptides that are used for silica synthesis in *Cylindrotheca fusiformis* [31], was introduced into the silk fibroin (thereafter referred to silk) hydrogel composites through enzymatic crosslinking. A well-controlled gradient distribution of the R5 peptide was achieved by regulating the peptide concentration along the longitudinal direction of the composites. The final gradient silicified silk/R5 (GSSR5) composites presented a structure with varied pore sizes and a gradient distribution of biosilica particles, similar to the structural features of natural osteochondral interfaces. More remarkably, these continuous gradient structures endowed the composites with gradient mechanical properties and distinct osteogenesis capacity. In addition, unlike chemical synthetic methods which use caustic chemicals [32–35], this simple and versatile approach allows for surface modification of biosilica particles to encapsulate biomolecules and drugs [36]. This novel gradient biomaterial design offers a useful approach to meet a broad range of needs in regenerative medicine involving osteochondral tissue engineering.

Materials and Methods

Materials

All chemical reagents used for making the GSSR5 composites were purchased from Sigma-Aldrich (St. Louis, MO, USA) unless otherwise specified. All materials and reagents used for cell culture and analysis were purchased from Thermo Fisher Scientific (Waltham, MA, USA) unless otherwise specified.

Preparation of aqueous silk solution

Silk solutions were prepared using our previously established procedures [37]. Briefly, ten grams of silk cocoons were cut into pieces and boiled in 4 L of 0.02 M sodium carbonate solution for 30 minutes to remove the coating of sericin protein. Degummed fibers were rinsed with deionized water three times and dried in air overnight. Five grams of dried fibers were dissolved in 20 ml of 9.3 M lithium bromide solution at 60°C for 4 hours. The silk fibroin solution was then dialyzed against deionized water using a dialysis cassette (Pierce 3.5 kDa MWCO; Fisher Scientific, PA) for 2 days. The solubilized silk solution was then centrifuged twice at 9,000 RPM, 4°C for 20 min to remove insoluble particulates. Protein concentration was determined by drying a known mass of the silk solution at 60°C for 12 hours and measuring the mass of the remaining solid.

Preparation of the gradient silk/R5 hydrogels

The biosilica selective peptide R5 (H-SSKKSGSYSGSKGSKRRIL-OH) with a purity of 95% was synthesized by GenScript (Piscataway, NJ, USA). Lyophilized horseradish peroxidase (HRP, type VI) powder and the R5 peptide powder were dissolved in deionized water to form a stock solution of 1,000 U/mL and 0.7 mg/μL, respectively. To generate the gradient silk/R5 hydrogels with high, medium and low loadings of the R5 peptide (thereafter referred to high, medium and low regions, respectively), the R5 peptide solution was first mixed with the silk solution in a R5/silk molar ratio of 250/1, 125/1 and 62.5/1, respectively. The mixture was then loaded sequentially into a cylindrical container layer by layer. First, the high region was loaded and gelation were initiated by adding the HRP and hydrogen peroxide (H_2O_2, 165 mM) solution at a ratio of 40 units and 40 μL per 1 mL of silk solution, respectively. Before the complete gelation in high region, the medium region was added on top of the high region followed by the addition of HRP and H_2O_2 with the same concentration as in the high region. Then the low region was added on top of the previous medium region followed by the addition of HRP and H_2O_2. The mixture was then incubated at 37°C overnight to ensure complete gelation. Unsilicified plain silk control hydrogels were prepared by crosslinking silk solution using HRP and H_2O_2 with the same ratio as in the gradient silk/R5 hydrogels.

Silicification

Biosilica deposition was introduced into the gradient silk/R5 hydrogels post gelation. Pre-hydrolyzed tetraethoxysilane (TEOS) solution was prepared by mixing 2.23 ml of TEOS solution with 7.76 ml of 50% ethanol/water solution, 10 μl of 1 M hydrogen chloride (HCl) and left at room temperature for 15 min. A 50 μl aliquot of the silk/R5 hydrogel was immersed in 200 μl silicifying medium consisting of 40 μl prehydrolyzed TEOS solution and 160 μl buffer solution (10.4 μl 1M bis-tris propane, 5.6 μl 1M citric acid solution and 144 μl deionized water) to allow for silicification at room temperature overnight. The silicifying medium was changed twice every 4 hours during the silicification process.

Fluorescence imaging of the FITC-labelled GSSR5 composites

The fluorescein isothiocyanate (FITC)-labelled R5 peptide (FITC-SSKKSGSYSGSKGSKRRIL-OH, GenScript, NJ, USA) was added into the R5 peptide solution in a molar ratio of 1 to 4,000. The resultant peptide mixture was used to create the FITC-labelled GSSR5 composites following the same gelation and silicification process as described earlier. The FITC-labelled composites were imaged using with the Olympus mvx10 macroscope and captured by cellSens Dimension (ver 1.8.1) program (Olympus, Tokyo, Japan).

Quantification of encapsulation efficiency

Quantification using FITC-labeled R5 peptide was performed to determine the encapsulation efficiencies of the R5 peptide in the GSSR5 composites. The FITC-R5 peptide was added into the R5 peptide solution in a molar ratio of 1 to 4,000 following the preparation process as described earlier. The silicifying medium was collected after silicification of the silk/R5 hydrogels. The amount of the FITC-R5 peptide in the supernatants was quantified by recording the emission signal using a SpectraMax M2e multimode microplate reader (Molecular Devices, CA, USA). All conjugation reactions were repeated in triplicate. The reaction efficiency was calculated as follows:

$$\text{Encapsulation efficiency} = \frac{\text{Peptide amount added} - \text{Peptide amount in supernatant}}{\text{Peptide amount added}} \times 100\%$$

Scanning Electron Microscopy (SEM) and Energy-dispersive X-ray Spectroscopy (EDS)

The gradient silicified silk/R5 hydrogel composites were frozen at −20°C and lyophilized. The samples were then quenched in liquid nitrogen, sputter coated with gold and imaged with a Carl Zeiss Ultra 55 field emission scanning electron microscope (Carl Zeiss SMT, Germany). Measurements of silica particle size were characterized by SEM. Energy dispersive X-ray analysis was used to determine the local composition of the samples (spectra of Si) over a depth of a few micrometers at different regions of the samples.

Fourier Transform Infrared Spectroscopy (FTIR)

Infrared spectroscopy of the lyophilized silicified silk/R5 hydrogel composites was performed with a Jasco FT/IR-6200 Spectrometer (Jasco, OK, USA), equipped with a deuterated triglycine sulfate detector (Pike Technologies, WI, USA). Unsilicified and silicified silk/R5 hydrogels with a silk/R5 molar ratio of 1/62.5 were prepared based on process described earlier and then frozen at −20°C and freeze dried for FTIR analysis. Each measurement incorporated 32 scans from 600 to 4000 cm^{-1} to yield spectra with a nominal resolution of 4 cm^{-1}. Fourier self-deconvolution (FSD) of the infrared spectra covering the Amide I region was performed with Opus 5.0 software (Bruker Optics Corp., MA, USA), as described previously [38,39]. The deconvoluted amide I bands were fitted with Gaussian peaks, and the ratio of the peak area of each secondary structure component to the total amide I band area were used to determine the fraction of each secondary structural element in the composites. Absorption bands in the range from 1590 to 1610 cm^{-1} relate to the side chain of amide I; bands from 1610 to 1637 cm^{-1} and from 1697 to 1703 cm^{-1} correlate to β-sheet structure; bands in the range from 1638 to 1652 cm^{-1} represent random coil, bands ranging from 1652 to 1660 cm^{-1} were ascribed to α-helices, and peaks in the range from 1660 to 1696 cm^{-1} were assigned to β-turn structures [38,40].

Mechanical tests

Unconfined compression tests were performed on the gradient silicified silk/R5 hydrogels between two impermeable plates using an Instron 3366 machine (Instron, MA, USA). The GSSR5 hydrogels were evenly cut to three sections along the longitude direction of the composites and tested separately as the low, medium and high regions of the hydrogels. The samples were subjected to a compressive ramp up to 15% strain at a strain rate 0.001 strain/s to obtain the stress-strain curves [41]. The 15% strain chosen here is within the physiological range for articular cartilage [7]. Compressive modulus was calculated as the slope of the curve from 5% to 10% strain. Five independent cylindrical samples (5 mm in height and 4 mm in diameter) were tested for each condition.

Cell Survival and proliferation

Human mesenchymal stem cells (hMSCs) were isolated from fresh bone marrow aspirate (Lonza, NJ, USA) from a healthy, non-smoking, young male as previously described [42]. HMSCs were cultured in expansion medium containing Dulbecco's modified eagle medium (DMEM) supplemented with 10% fetal bovine serum (FBS), 1% non-essential amino acids, 1% antibiotic/antimycotic (100U mL^{-1} penicillin, 100 μg mL^{-1} streptomycin, 0.25μg mL^{-1} fungizone) and 1 ng/ml fibroblast growth factor-basic (bFGF). For cell seeding, gradient silicified silk/R5 hydrogels were frozen at −20°C, lyophilized and autoclaved for sterilization. Cells at passage 2–3 were seeded at 1 million per GSSR5 composite (50 μl volume), and allowed to attach for 1 hours prior to flooding the composites with growth media. The growth medium contained DMEM supplemented with 10% FBS, 1% non-essential amino acids and 1% antibiotic/antimycotic. All cell cultures were incubated at 37°C supplemented with 5% CO_2. After 24 hours, the cultures were switched to osteogenic differentiation medium consisting of DMEM with 10% FBS, 1% antibiotics-antimycotic, 1% non-essential amino acids, 10 mM β-glycerol-2-phosphate (Sigma-Aldrich), 100 nM dexamethasone (Sigma-Aldrich), and 0.05 mM L-ascorbic acid (Sigma-Aldrich). The medium was changed every 2–3 days. Unsilicified plain silk hydrogel scaffolds served as controls. Following the manufacturer’s protocol, hMSC proliferation in the composites was monitored by Alamar blue dye reduction assay. Viable cells in the composites after 19-day culture were observed using a live/dead assay kit. The actin expression of hMSCs in three-dimensional (3D) cell culture was visualized by fluorescence F-actin staining following the manufacturer's instructions.

Histology

The samples were harvested after 6 weeks of culture in osteogenic media and fixed in 4% phosphate-buffered saline (PBS)-buffered paraformaldehyde at 4°C overnight. The samples were then dehydrated through graded ethanol (70%, 90%, 95% and 100%), embedded in paraffin and sectioned at 8 μm thickness. Hematoxylin and eosin (H&E) staining was performed based on standard histochemical techniques. Calcium deposition was analyzed using the von Kossa stain method [43]. Sirius red staining was performed using the Picro-Sirius red stain kit (Abcam, UK) according to the manufacturer's instructions for the assessment of collagen fibers. Samples were imaged using a BZ-X700 series microscope (Keyence, IL, USA).

Osteogenic gene expression

Samples were collected at desired time points, rinsed in PBS and stored in TRIzol reagent at −80°C until analysis. Total RNA was isolated using the PureLink® RNA Mini Kit. The RNA was reverse-transcribed to synthesize cDNA using the High Capacity cDNA Reverse Transcription Kit according to manufacturer's instructions. Real-time PCR amplification was performed on 1 μg cDNA using TaqMan® Universal PCR Master Mix with an ABI Prism 7000 Sequence Detection System (Applied Biosystems, USA). Primer sequences from TaqMan® Gene Expression Assays included the housekeeping gene glyceraldehyde 3-phosphate dehydrogenase (GAPDH, Hs99999905_m1), osteogenic genes Runt-related transcription factor 2 (Runx2, Hs00231692_m1), collagen type I (Col1, Hs00164004_m1), alkaline phosphatase (ALP, Hs01029144_m1), and bone sialoprotein (BSP, Hs00173720_m1). Gene expression was normalized to GAPDH using the comparative Ct ($2^{-\Delta\Delta Ct}$) method.

Statistical analysis

Paired or unpaired Student t-tests, as appropriate, were used to determine statistical differences between groups. One-way ANOVA was used when comparing features between groups. In all cases, $n > 3$ were used for data sets ($p < 0.05$ or 0.01). GraphPad software (GraphPad Prism software, CA) was utilized.

Results

The strategy for design and synthesis of the gradient protein/biosilica composites

Biomimetic mineralization is a process by which natural organisms deposit minerals in an organized manner on the organic templates, leading to functional materials with desired hierarchical structures [44,45]. During the formation of siliceous spicules in sponges (also well-known as *in vivo* silicification, as sketched in Figure 1A), central protein filaments consisting of silicatein and scaffold protein first self-assemble in the extracellular space. Silicatein then triggers and mediates the deposition of biosilica particles on a fibrous network of collagen, which subsequently form concentric lamellar layers around the filament [46]. To mimic this natural biomineralization process, silk protein was chosen to construct the 3D continuous porous structure due to its biocompatibility, degradability and tunable mechanical properties [47]. The silk protein was enzymatically crosslinked via HRP and H_2O_2 to form a hydrogel [47], acting as templates to mimic the function of collagen and other scaffold protein in nature [22,46]. The R5 peptides were simultaneously crosslinked into the silk templates to trigger and mediate the *in situ* biomineralization in the GSSR5 composites (Figure 1B). The spatial variation of silicification was achieved by varying the molar ratio of the R5/silk along the longitudinal direction of the composites (Figure 1C). The mixture of the high, medium and low regions of the GSSR5 composites were loaded sequentially into a cylindrical mold layer by layer, followed by the addition of HRP and H_2O_2 to initiate gelation. The gradient distribution of the mineralization domains allows for tunable control over the morphology, self-assembly and distribution of biosilica particles and ultimately regulation of the mechanical and structural properties and architecture of the gradient composites.

The final hydrogels appeared free-standing and uniform without any cracks (Figure 1D). Their gradient structures were confirmed by fluorescence imaging of the GSSR5 composites containing immobilized FITC-labeled R5 peptides and encapsulation efficiency measurements. The GSSR5 composites displayed an increasing fluorescence signal of FITC-R5 along the longitudinal direction of the composites (Figure 1C), indicating the increasing content of the R5 peptide along the trend. The fluorescence intensity along the gradient trend of the FITC-R5 in the GSSR5 composites were measured (Figure S1C, Supplementary material), indicating the continuous gradient evidence in the composites. Figure 1E shows the quantification of the R5 peptide in different regions of the GSSR5 composites. The R5 peptide were loaded into the low, medium and high regions of the GSSR5 composites with a synthesis silk/R5 molar ratio of 1/62.5, 1/125 and 1/250, respectively, whereas the R5 peptide encapsulated in the low, medium and high regions of the composites after silicification had a final silk/R5 molar ratio of 1/60, 1/121, 1/205, respectively. The slight difference is because some weakly attached R5 peptides were released into the silicifying medium during *in vitro* silicification. According to the encapsulation efficiency assay, the percentage of the released peptides in the low, medium and high regions were 3.8±2.0%, 3.2±1.4% and 7.9±3.3%, respectively, while the encapsulation efficiencies of the low, medium and high regions in the GSSR5 composites were 96.2±2.0%, 96.8±1.4%, and 92.1±3.3%, respectively (Table 1).

Structural and mechanical properties of the GSSR5 composites

To examine the mesoscopic structures of the GSSR5 composites, SEM measurements were performed on the freeze-dried GSSR5 composites (Figure 2A–F). Freeze-drying process was performed on the materials to create a favorable heterogeneous matrix of pore structure for cell culture. The final GSSR5 composites exhibited uniform porous structure in three regions, while with different pore sizes. The pore sizes gradually decreased from the low region to the high region in the GSSR5 composites. The pore sizes in the low regions were significantly larger than those in the medium regions ($p<0.01$), which were larger than those in the high regions in the gradient composites (Figure S2, Supplementary material, $p<0.05$). In addition, the gradient distribution of biosilica particles was observed (Figure 2D–F). Spherical silica particles (760±130 nm in diameter, Figure 2F) were embedded in the silk/R5 network giving rise to a rough granular appearance superimposed on the bio-template network, indicating the silicification function of the R5 peptide was maintained upon grafting to the silk templates. More importantly, the amount of biosilica significantly increased by increasing of the loading of the R5 peptide, which was further confirmed by EDS tests (the insert images in Figure 2D–F). The silica densities in the low regions were significantly lower than those in the medium regions, which were lower than those in the high regions in the gradient composites (Figure S3, Supplementary material, $p<0.05$). The molar percentage of silicon increased from low to high R5 peptide loading region, with values of 1.1%, 1.5% and 2.3% of low, medium and high regions, respectively, as determined by silicon test colorimetric assay (Figure S4, Supplementary material). The Si distribution along the gradient composites were generated using EDS mapping (Figure S1D, Supplementary material), which further confirmed the continuous gradient silicification in the composites.

Compression tests were carried out to assess the mechanical performance of the GSSR5 composites, as shown in Figure 3, the gradient biosilica content in the protein network endowed gradient mechanical behaviors. The GSSR5 composites with low, medium and high loadings of the R5 peptide were evenly sectioned into three regions along the longitude direction of the composites, whose representative stress-strain curves were shown in Figure 3A. The calculated compressive Young's moduli of the low, medium and high regions in the GSSR5 composites were 20.7 ± 5.0 kPa, 49.5 ± 10.6 kPa and 128.5 ± 16.4 kPa, respectively (Figure 3B). The results showed that a 2-fold increase of biosilica content from low to high regions led to an approximately 6-fold increase in the compressive Young's moduli, indicating that the stiffening effect of biosilica was achieved. The compressive modulus of the low region was significantly lower than that of the medium region ($p<0.05$), which was again significantly lower than that of the high region in the GSSR5 composites ($p<0.01$).

FTIR spectroscopy was used to investigate the secondary structure of the protein/biosilica composites. Figure 4 shows the amide I bands in the FTIR spectra of the silk/R5 composites before (Figure 4A) and after (Figure 4B) silicification. The peaks at 1644 cm^{-1}, 1656 cm^{-1} and 1675 cm^{-1} indicate that the non-crystalline structures, such as random coil (1638–1652 cm^{-1}), α-helix (1652–1660 cm^{-1}) and β-turns (1660 to 1696 cm^{-1}) [38,40] dominated in the unsilicified silk/R5 composites (Figure 4A), which simultaneously diminished in the silicified composites (Figure 4B). After silicification, the intensity of β-sheet crystalline peak at 1621 cm^{-1} increased in the composites, indicating an increase of the β-sheet content after silicification (Figure 4A, B). The content of β-sheet increased after silicification (from $36\pm3\%$ to $48\pm4\%$) while the content of non-crystalline structures decreased (α-helix: from $12\pm2\%$ to $10\pm1\%$; random coil: from $22\pm2\%$ to $18\pm2\%$) (Figure 4C). Recent work has characterized the secondary structure of the R5 peptide during silicification. The R5 peptide was characterized as a disparate random coil ensemble in solution, which remain unchanged in the presence of silicic acid solution [48]. The increase of beta sheet content in the GSSR5 composites after silicification was due to the formation of crystalline structure in silk protein [49].

Cytocompatibility evaluation of the GSSR5 composites

The lyophilized GSSR5 composites with gradient matrix pore structure were seeded with hMSCs to guide cell growth and proliferation and to evaluate the cytocompatibility of the composites in comparison with uniform silk/R5 composites and unsilicified plain silk controls. After a 19-day culture, hMSCs exhibited favorable metabolic activity, spread out their actin filaments and aligned with the pores of the composites with uniform distribution (Figure 5A, D). Alamar blue assay showed comparable proliferation of hMSCs in the gradient, uniform and control groups during the culture (Figure 5E). There was a significant increase of fluorescence intensity from day 3 to day 15 indicating favorable cell proliferation in all groups during the culture period ($p<0.01$). Strong green fluorescence with minimal visible red fluorescence (Figure 5B–D) was detected from the live/dead staining of hMSCs in the GSSR5 composites during the culture, indicating the cytocompatibility of the material.

The GSSR5 composites offered tunable osteogenic differentiation and calcium deposition in 3D cell culture

HMSCs were seeded into the lyophilized GSSR5 composites and unsilicified plain silk controls and cultured under osteogenic conditions for 6 weeks. H&E staining revealed heterogeneous cell morphologies, e.g., enlarged cuboidal cells in the regions with high peptide loading, while most cells remained undifferentiated with a more elongated shape in the regions with low peptide loading, as well as in the unsilicified plain silk controls (Figure 6A–D).

Von Kossa staining revealed increased calcification in the GSSR5 composites with high loading of peptide, compared to the medium and low loadings and to the controls (Figure 6E–H). Histological analysis revealed that hMSCs cultured in high regions deposited minerals more intensely which clustered in the interstitial spaces of the pores and extended to the walls of the pores, while the medium and low regions showed less mineral deposition. Unsilicified controls showed minimal staining of calcium. The area ratio of calcium staining in the low regions were significantly lower than those in the medium regions, which were lower than those in the high regions in the gradient composites (Figure S5, Supplementary material, $p<0.01$). Sirius red staining confirmed the secretion of collagen fibers in the GSSR5 composites (Figure 6J, K, L), whereas minimal collagen fibers were present in the controls (Figure 6I). The deposition of bone-specific ECM in the gradient composites was evidenced by immunofluorescence staining of collagen type I which is the major bone matrix component [50,51]. Regions with high loading of the peptides showed stronger expression of collagen type I compared to the medium regions, while minimum expression of collagen type I was observed in the low regions of the gradient composites as well as in the controls (Figure S6, Supplementary material). Bone-like tissue formation was supported within the high region of the composites, while most cells remained in undifferentiated state in the low region. The cells differentiated along the composites in a manner consistent with the R5-gradient profile (Figure 6M).

After six weeks of culture, strong transcript levels of bone markers (Runx2, collagen type I, ALP and BSP) were observed in hMSCs cultured in the lyophilized GSSR5 composites and uniform silk/R5 composites compared to the unsilicified silk controls represented by the baseline (Figure 7). A significant increase in Runx2 transcript levels in the GSSR5 and uniform composites was observed after 6 weeks ($p < 0.05$) (Figure 7A), supporting the commitment of these composites to induce hMSC differentiation toward the osteogenic lineage. The expression of collagen type I, the most abundant extracellular matrix protein in bone, was comparable between all four groups after 6-week culture (Figure 7B). The expression of alkaline phosphatase was up-regulated by 2-fold in regions with high loading compared with that in the controls (Figure 7C), indicating advanced osteoblast development and matrix maturation to prepare for mineralization in the high region [52]. Moreover, the expression of BSP, the late-stage osteogenic differentiation marker, was significantly improved in the GSSR5 and uniform composites than that in the controls after 6 weeks ($p < 0.05$, Figure 7D), which further supported the upregulation of osteogenesis in these composites.

In summary, when seeded with hMSCs and cultured in osteogenic medium, the GSSR5 composites showed elevated transcript levels of the osteogenic genes, increased collagen secretion and calcium deposition when compared with the unsilicified silk controls. Increased osteogenic gene expression corroborates the development of advanced osteoblasts, the maturation of extracellular matrix and mineral accumulation [53].

Discussion

The GSSR5 composites combined two key structural properties–strength of the protein templates and toughness of biosilica. Biosilica can effectively stimulate osteoblast differentiation, inhibit osteoclastic activity and enhance mineral deposition in bone tissue [54]. However, the degradability of biosilica is limited, and the materials by themselves are brittle, which make it difficult to generate useful 3D materials [55,56]. To solve these problems, several silk/R5/biosilica composites [57–59] have been developed for osteogenesis in the form of two-dimensional (2D) films, due to the excellent biocompatibility [60–62], tunable mechanical properties [47], and low inflammatory response [63,64] of silk. In these systems, the R5 peptide has been either genetically [57–59,65] or chemically [65] fused to the silk to control the assembly and deposition of the silica particles in the silk films for osteogenesis. The R5 peptide contains lysine residues which are crucial in mediating the polycondensation of silica nanospheres during silicification [66,67]. Previous work has demonstrated that the R5 peptides promoted the intermolecular interactions of biosilica particles and the peptide. The hydrophobic nature of the R5 peptide led to entropically favored peptide aggregates, while the positively charged residues on the R5 peptide activated silica precipitation through an electron-donor-acceptor mechanism [67,68]. The combination of the silk and silica promoted the osteogenic differentiation of hMSCs and enhanced nodular mineral deposits on the films. Biosilica also accelerated cell proliferation, upregulating osteoprotegerin (OPG) and bone morphogenetic protein 2 (BMP2) expression in osteogenic cells on silicatein/biosilica-modified substrates [69]. However, several problems still exist, as 2D systems fail to mimic the complex cellular environments *in vivo* [70]. Moreover, constructs with uniform physical and chemical properties lack the spatially and structurally defined hierarchical architecture that exists in native tissues and fail to recreate the natural graded interface [4].

In this study, GSSR5 composites obtained continuous variation in compositional, physiological and mechanical properties and created 3D biomimetic cellular niches for osteogenic differentiation to better mimic the complex cellular environments *in vivo* with more representative response to the external stimuli in the surroundings [70,71]. More importantly, these combined gradients not only offered a favorable platform to template mineral deposition, but also provided a suitable process that reproduced the role of cells. The variation in mineralization, together with the structural and mechanical gradients, triggered the cells to promote localized mineralization within the matrix. Cells deposited minerals to the protein/biosilica matrix which further strengthened and hardened the material itself. Bone-like tissue formation was supported within the subchondral end of the composites (high region), while most cells remained in undifferentiated state in the low region. The spatial osteogenesis of hMSCs along the gradient composites was confirmed by the heterogeneous cell morphologies and varied calcification from the histology results, the gradient expression of collagen type I as well as the elevated transcript levels of selective bone markers in the GSSR5 composites.

In the protein/biosilica composites, the mineralization domains acted as special loci to support the formation and accumulation of HA crystallites with small size and low crystallinity, which are important for the biochemistry of biomineralization [72]. Biosilica bound to the mineralization domains were immobilized in the silk matrix and induced the collagen synthesis [58,69,73,74]. Collagen fibers then further promoted the mineral deposition and bound to apatite crystals resulting in intercalating mineral structure [72,75,76]. Upon the formation of the apatite nuclei, spontaneous growth of apatite occurred by the addition of calcium and phosphate ions from surrounding medium. The features above derived from the molecular-level organic-inorganic interfaces were established by the presence of the R5 peptide template, combined with the regional control of such chemistries within the gradient design.

The GSSR5 composites also transmitted favorable gradient physical stimuli including mechanics, mass and architecture to cells towards osteogenic lineage. These GSSR5 composites exhibited gradient pore microstructures, large pore size and an interconnected pore structure which affected the osteogenic differentiation through various aspects, notably surface area, matrix deposition and nutrient diffusion [77]. Enhanced osteogenesis was observed in the stiffer regions of the GSSR5 composites. This mechanical stimulus, via matrix stiffness, could affect cellular distribution, metabolic activity and the ultimate mechanics of the tissue itself [78,79]. The stem cells differentiating towards osteogenic lineage adhered better to rigid substrates and tended to form mineralized nodules on rough surfaces [77]. More information is needed to establish whether differential cell behaviors were due to the biomimetic cues (the R5 peptide, biosilica), the mechanical transitions or the architectures of the composites.

The soft tissue-bone tissue interface is characterized by an elevated level of heterogeneous structural architecture to facilitate joint function [80–82]. This gradient protein/biosilica system holds benefits in supporting cell growth and differentiation, mimicking the native matrix heterogeneity and exhibiting tunable mechanics, which make it a promising strategy design for interfacial tissue repair. However, limitations in soft tissue-bone repair would need to be addressed before the gradient composites can be used *in vivo*. For example, tendon-bone interface repair exhibits significant clinical challenges in promoting the biological fixation of the engineered grafts with the implant sites and facilitating the functional integration of tendon with bone after injury. Such fixation requires the engineered graft to be pre-incorporated into the strategic design of the replacement grafts in order to restore the function of the tissue interfaces [82–84].

In summary, such composite materials can be used to study the growth of natural tissues and the processes of regeneration, but also to act as tissue engineering constructs *in vitro* and *in vivo*, such as for osteochondral plugs. Silk-based materials offered beneficial hydrophilicity for cell adhesion and survival, while also maintaining appropriate swelling ratios to avoid scaffold deformation (Figure S7, S8, Supplementary material), as demonstrated in previous work [77,85–87]. The biocompatibility of the silk-based materials has been demonstrated *in vivo* previously. Silk hydrogels enzymatically crosslinked by HRP and H_2O_2 were implanted subcutaneously in a mouse model and showed progressive cell infiltration and degradation [47]. Also, the system can be easily scaled up to match the dimension of critical osteochondral defects. To this end, further optimization would be useful, such as to: 1) extend the range of mechanics through increasing the silk concentration and molecular weight within the composites. The highest mechanics obtained in the GSSR5 composites may not reach that of the native bone, as the stiffness of fresh cancellous human bone is around 700 MPa [88]. However, the scaffold could be supported by the surrounding bone and invaded by the formation of new bone during degradation; 2) investigate chondrogenesis in this type of system. The formation of the proteoglycan-rich matrix in the gradient composites indicated that these composites supported the formation of cartilaginous-like tissue (Figure S9, Supplementary material).

More importantly, the incorporation of biosilicification domains into the biocompatible silk substrates under mild (peptide-mediated) conditions provides other potential applications. Surface modifications of the inert biosilica particles would allow for encapsulation of biomolecules, e.g., enzymes, and drugs which are sensitive to heat or caustic chemicals [36]. The incorporation of biosilicification domains into the silk substrates also provides opportunities to encapsulate various functional peptides and molecules. For example, a variety of polycationic peptides e.g. silaffin that are able to precipitate silica nanospheres individually can be encapsulated in the silk substrates, leading to advanced functional materials with different mineral morphology and organization [31,89]. Depending on the peptide used for biomineralization and the external physical/chemical stimuli, different silica structures can be generated including sphere-like (with R5), fibrous structures (with p-(lys)1642) and platelike (with p-(lys)189) *in vitro* [90]. This novel gradient biomaterial design offers a useful approach to meet a broad range of needs in regenerative medicine involving interfacial tissue engineering.

Conclusions

3D GSSR5 composites were developed through integration of enzymatically triggered protein gelation and R5-induced gradient silicification. This composite system offers continuous transitions in terms of composition, structure and mechanical properties as well as cytocompatibility and biodegradability. The GSSR5 composites were competent to promote and regulate the osteogenic differentiation of human mesenchymal stem cells in an osteoinductive environment. The cells differentiated along the composites in a manner consistent with the R5-gradient profile. This novel biomaterial design offers a promising strategy to meet a broad range of needs in regenerative medicine involving osteochondral tissue engineering, as well as graded tissue interfaces. Furthermore, this strategy offered a platform to create clinically relevant tissue engineered composites through encapsulating other functional molecules and proteins and to screen for optimal doses and combinations in a 3D environment.

Supplementary Material

Refer to Web version on PubMed Central for supplementary material.

Acknowledgments

Funding: This work was supported by the National Institutes of Health [4R01DE017207-09, 2R01DE016525-08].

References

1. Mikos AG, Herring SW, Ochareon P, Elisseeff J, Lu HH, Kandel R, Schoen FJ, Toner M, Mooney D, Atala A, Van Dyke ME, Kaplan D, Vunjak-Novakovic G. Engineering complex tissues. Tissue Eng. 2006; 12:3307–39. DOI: 10.1089/ten.2006.12.3307 [PubMed: 17518671]
2. Singh M, Berkland C, Detamore MS. Strategies and applications for incorporating physical and chemical signal gradients in tissue engineering. Tissue Eng Part B Rev. 2008; 14:341–66. DOI: 10.1089/ten.teb.2008.0304 [PubMed: 18803499]
3. Buckwalter JA, Mankin HJ. Articular cartilage: tissue design and chondrocyte-matrix interactions. Instr Course Lect. 1998; 47:477–86. http://www.ncbi.nlm.nih.gov/pubmed/9571449. [PubMed: 9571449]
4. Di Luca A, Van Blitterswijk C, Moroni L. The osteochondral interface as a gradient tissue: from development to the fabrication of gradient scaffolds for regenerative medicine. Birth Defects Res C Embryo Today. 2015; 105:34–52. DOI: 10.1002/bdrc.21092 [PubMed: 25777257]
5. Bhosale AM, Richardson JB. Articular cartilage: structure, injuries and review of management. Br Med Bull. 2008; 87:77–95. DOI: 10.1093/bmb/ldn025 [PubMed: 18676397]
6. Zizak I, Roschger P, Paris O, Misof B, Berzlanovich A, Bernstorff S, Amenitsch H, Klaushofer K, Fratzl P. Characteristics of mineral particles in the human bone/cartilage interface. J Struct Biol. 2003; 141:208–217. DOI: 10.1016/S1047-8477(02)00635-4 [PubMed: 12648567]
7. Schinagl RM, Gurskis D, Chen AC, Sah RL. Depth-dependent confined compression modulus of full-thickness bovine articular cartilage. J Orthop Res. 1997; 15:499–506. DOI: 10.1002/jor.1100150404 [PubMed: 9379258]
8. van Dijk CN, Reilingh ML, Zengerink M, van Bergen CJA. Osteochondral defects in the ankle: why painful?, Knee Surgery. Sport Traumatol Arthrosc. 2010; 18:570–580. DOI: 10.1007/s00167-010-1064-x
9. Tampieri A, Sprio S, Sandri M, Valentini F. Mimicking natural bio-mineralization processes: A new tool for osteochondral scaffold development. Trends Biotechnol. 2011; 29:526–535. DOI: 10.1016/j.tibtech.2011.04.011 [PubMed: 21645938]
10. Shimomura K, Moriguchi Y, Murawski CD, Yoshikawa H, Nakamura N. Osteochondral tissue engineering with biphasic scaffold: current strategies and techniques. Tissue Eng Part B Rev. 2014; 20:468–76. DOI: 10.1089/ten.TEB.2013.0543 [PubMed: 24417741]
11. Schek RM, Taboas JM, Segvich SJ, Hollister SJ, Krebsbach PH. Engineered osteochondral grafts using biphasic composite solid free-form fabricated scaffolds. Tissue Eng. n.d; 10:1376–85. DOI: 10.1089/ten.2004.10.1376 [PubMed: 15588398]

12. Li JJ, Kim K, Roohani-Esfahani SI, Guo J, Kaplan DL, Zreiqat H. A biphasic scaffold based on silk and bioactive ceramic with stratified properties for osteochondral tissue regeneration. J Mater Chem B Mater Biol Med. 2015; 3:5361–5376. DOI: 10.1039/C5TB00353A [PubMed: 26167284]
13. Da H, Jia SJ, Meng GL, Cheng JH, Zhou W, Xiong Z, Mu YJ, Liu J. The Impact of Compact Layer in Biphasic Scaffold on Osteochondral Tissue Engineering. PLoS One. 2013; 8:e54838.doi: 10.1371/journal.pone.0054838 [PubMed: 23382984]
14. Grayson WL, Bhumiratana S, Grace Chao PH, Hung CT, Vunjak-Novakovic G. Spatial regulation of human mesenchymal stem cell differentiation in engineered osteochondral constructs: effects of pre-differentiation, soluble factors and medium perfusion. Osteoarthr Cartil. 2010; 18:714–23. DOI: 10.1016/j.joca.2010.01.008 [PubMed: 20175974]
15. Levingstone TJ, Matsiko A, Dickson GR, O'Brien FJ, Gleeson JP. A biomimetic multilayered collagen-based scaffold for osteochondral repair. Acta Biomater. 2014; 10:1996–2004. DOI: 10.1016/j.actbio.2014.01.005 [PubMed: 24418437]
16. Jeon JE, Vaquette C, Klein TJ, Hutmacher DW. Perspectives in multiphasic osteochondral tissue engineering. Anat Rec (Hoboken). 2014; 297:26–35. DOI: 10.1002/ar.22795 [PubMed: 24293311]
17. Aydin HM. A Three-Layered Osteochondral Plug: Structural, Mechanical, and in vitro Biocompatibility Analysis. Adv Eng Mater. 2011; 13:B511–B517. DOI: 10.1002/adem.201180005
18. Nooeaid P, Roether JA, Weber E, Schubert DW, Boccaccini AR. Technologies for Multilayered Scaffolds Suitable for Interface Tissue Engineering. Adv Eng Mater. 2014; 16:319–327. DOI: 10.1002/adem.201300072
19. Wang X, Wenk E, Zhang X, Meinel L, Vunjak-Novakovic G, Kaplan DL. Growth factor gradients via microsphere delivery in biopolymer scaffolds for osteochondral tissue engineering. J Control Release. 2009; 134:81–90. DOI: 10.1016/j.jconrel.2008.10.021 [PubMed: 19071168]
20. Mohan N, Dormer NH, Caldwell KL, Key VH, Berkland CJ, Detamore MS. Continuous gradients of material composition and growth factors for effective regeneration of the osteochondral interface. Tissue Eng Part A. 2011; 17:2845–55. DOI: 10.1089/ten.tea.2011.0135 [PubMed: 21815822]
21. Woodfield TBF, Malda J, de Wijn J, Péters F, Riesle J, van Blitterswijk CA. Design of porous scaffolds for cartilage tissue engineering using a three-dimensional fiber-deposition technique. Biomaterials. 2004; 25:4149–61. DOI: 10.1016/j.biomaterials.2003.10.056 [PubMed: 15046905]
22. Roach HI. Why does bone matrix contain non-collagenous proteins? The possible roles of osteocalcin, osteonectin, osteopontin and bone sialoprotein in bone mineralisation and resorption. Cell Biol Int. 1994; 18:617–28. DOI: 10.1006/cbir.1994.1088 [PubMed: 8075622]
23. Khanarian NT, Haney NM, Burga RA, Lu HH. A functional agarose-hydroxyapatite scaffold for osteochondral interface regeneration. Biomaterials. 2012; 33:5247–5258. DOI: 10.1016/j.biomaterials.2012.03.076 [PubMed: 22531222]
24. Oliveira JM, Rodrigues MT, Silva SS, Malafaya PB, Gomes ME, Viegas CA, Dias IR, Azevedo JT, Mano JF, Reis RL. Novel hydroxyapatite/chitosan bilayered scaffold for osteochondral tissue-engineering applications: Scaffold design and its performance when seeded with goat bone marrow stromal cells. Biomaterials. 2006; 27:6123–6137. DOI: 10.1016/j.biomaterials.2006.07.034 [PubMed: 16945410]
25. Bhumiratana S, Grayson WL, Castaneda A, Rockwood DN, Gil ES, Kaplan DL, Vunjak-Novakovic G. Nucleation and growth of mineralized bone matrix on silk-hydroxyapatite composite scaffolds. Biomaterials. 2011; 32:2812–2820. DOI: 10.1016/j.biomaterials.2010.12.058 [PubMed: 21262535]
26. Dorozhkin SV, Epple M. Biological and Medical Significance of Calcium Phosphates. Angew Chemie Int Ed. 2002; 41:3130–3146. DOI: 10.1002/1521-3773(20020902)41:17<3130::AID-ANIE3130>3.0.CO;2-1
27. Zhang Q. Dissolution and mineralization behaviors of HA coatings. Biomaterials. 2003; 24:4741–4748. DOI: 10.1016/S0142-9612(03)00371-5 [PubMed: 14530071]
28. Tampieri A, Sandri M, Landi E, Pressato D, Francioli S, Quarto R, Martin I. Design of graded biomimetic osteochondral composite scaffolds. Biomaterials. 2008; 29:3539–3546. DOI: 10.1016/j.biomaterials.2008.05.008 [PubMed: 18538387]

29. Beniash E. Biominerals-hierarchical nanocomposites: the example of bone. Wiley Interdiscip Rev Nanomedicine Nanobiotechnology. 2011; 3:47–69. DOI: 10.1002/wnan.105 [PubMed: 20827739]
30. Yang PJ, Temenoff JS. Engineering orthopedic tissue interfaces. Tissue Eng Part B Rev. 2009; 15:127–41. DOI: 10.1089/ten.teb.2008.0371 [PubMed: 19231983]
31. Kröger N, Deutzmann R, Sumper M. Polycationic Peptides from Diatom Biosilica That Direct Silica Nanosphere Formation. Science (80-). 1999; 286:1129–1132. DOI: 10.1126/science.286.5442.1129
32. Gill I, Ballesteros A. Bioencapsulation within synthetic polymers (Part 1): sol-gel encapsulated biologicals. Trends Biotechnol. 2000; 18:282–96. http://www.ncbi.nlm.nih.gov/pubmed/10950510. [PubMed: 10950510]
33. Gill I, Ballesteros A. Encapsulation of Biologicals within Silicate, Siloxane, and Hybrid Sol-Gel Polymers: An Efficient and Generic Approach. J Am Chem Soc. 1998; 120:8587–8598. DOI: 10.1021/ja9814568
34. Lawson AC, Czernuszka JT. Collagen-calcium phosphate composites. Proc Inst Mech Eng Part H J Eng Med. 1998; 212:413–425. DOI: 10.1243/0954411981534187
35. Xu AW, Ma Y, Cölfen H. Biomimetic mineralization. J Mater Chem. 2007; 17:415–449. DOI: 10.1039/B611918M
36. Luckarift HR, Spain JC, Naik RR, Stone MO. Enzyme immobilization in a biomimetic silica support. Nat Biotechnol. 2004; 22:211–213. DOI: 10.1038/nbt931 [PubMed: 14716316]
37. Rockwood DN, Preda RC, Yücel T, Wang X, Lovett ML, Kaplan DL. Materials fabrication from Bombyx mori silk fibroin. Nat Protoc. 2011; 6:1612–31. DOI: 10.1038/nprot.2011.379 [PubMed: 21959241]
38. Hu X, Kaplan D, Cebe P. Determining Beta-Sheet Crystallinity in Fibrous Proteins by Thermal Analysis and Infrared Spectroscopy. Macromolecules. 2006; 39:6161–6170. DOI: 10.1021/ma0610109
39. Huang W, Krishnaji S, Hu X, Kaplan D, Cebe P. Heat Capacity of Spider Silk-Like Block Copolymers. Macromolecules. 2011; 44:5299–5309. DOI: 10.1021/ma200563t [PubMed: 23869111]
40. Jung C. Insight into protein structure and protein-ligand recognition by Fourier transform infrared spectroscopy. J Mol Recognit. 2000; 13:325–51. DOI: 10.1002/1099-1352(200011/12)13:6<325::AID-JMR507>3.0.CO;2-C [PubMed: 11114067]
41. DiSilvestro MR, Suh JKF. A cross-validation of the biphasic poroviscoelastic model of articular cartilage in unconfined compression, indentation, and confined compression. J Biomech. 2001; 34:519–525. DOI: 10.1016/S0021-9290(00)00224-4 [PubMed: 11266676]
42. Li C, Hotz B, Ling S, Guo J, Haas DS, Marelli B, Omenetto F, Lin SJ, Kaplan DL. Regenerated silk materials for functionalized silk orthopedic devices by mimicking natural processing. Biomaterials. 2016; 110:24–33. DOI: 10.1016/j.biomaterials.2016.09.014 [PubMed: 27697669]
43. Sheehan, D., Hrapchak, B. Theory and practice of histotechnology. C. V. Mosby Co; St. Louis, MO: 1973.
44. Xu G, Yao N, Aksay IA, Groves JT. Biomimetic Synthesis of Macroscopic-Scale Calcium Carbonate Thin Films. Evidence for a Multistep Assembly Process. J Am Chem Soc. 1998; 120:11977–11985. DOI: 10.1021/ja9819108
45. Mann S. Molecular recognition in biomineralization. Nature. 1988; 332:119–124. DOI: 10.1038/332119a0
46. Müller WEG, Wang X, Cui FZ, Jochum KP, Tremel W, Bill J, Schröder HC, Natalio F, Schloβmacher U, Wiens M. Sponge spicules as blueprints for the biofabrication of inorganic–organic composites and biomaterials. Appl Microbiol Biotechnol. 2009; 83:397–413. DOI: 10.1007/s00253-009-2014-8 [PubMed: 19430775]
47. Partlow BP, Hanna CW, Rnjak-Kovacina J, Moreau JE, Applegate MB, Burke KA, Marelli B, Mitropoulos AN, Omenetto FG, Kaplan DL. Highly tunable elastomeric silk biomaterials. Adv Funct Mater. 2014; 24:4615–4624. DOI: 10.1002/adfm.201400526 [PubMed: 25395921]
48. Senior L, Crump MP, Williams C, Booth PJ, Mann S, Perriman AW, Curnow P. Structure and function of the silicifying peptide R5. J Mater Chem B. 2015; 3:2607–2614. DOI: 10.1039/C4TB01679C

49. Ling S, Qi Z, Knight DP, Shao Z, Chen X. Synchrotron FTIR Microspectroscopy of Single Natural Silk Fibers. Biomacromolecules. 2011; 12:3344–3349. DOI: 10.1021/bm2006032 [PubMed: 21790142]
50. Viguet-Carrin S, Garnero P, Delmas PD. The role of collagen in bone strength. Osteoporos Int. 2006; 17:319–336. DOI: 10.1007/s00198-005-2035-9 [PubMed: 16341622]
51. Kim HJ, Kim UJ, Kim HS, Li C, Wada M, Leisk GG, Kaplan DL. Bone tissue engineering with premineralized silk scaffolds. Bone. 2008; 42:1226–1234. DOI: 10.1016/j.bone.2008.02.007 [PubMed: 18387349]
52. Lian JB, Stein GS. Development of the osteoblast phenotype: molecular mechanisms mediating osteoblast growth and differentiation. Iowa Orthop J. 1995; 15:118–140. [PubMed: 7634023]
53. Clarke B. Normal bone anatomy and physiology. Clin J Am Soc Nephrol. 2008; 3(Suppl 3):S131–9. DOI: 10.2215/CJN.04151206 [PubMed: 18988698]
54. Beck GR, Ha SW, Camalier CE, Yamaguchi M, Li Y, Lee JK, Weitzmann MN. Bioactive silica-based nanoparticles stimulate bone-forming osteoblasts, suppress bone-resorbing osteoclasts, and enhance bone mineral density in vivo. Nanomedicine. 2012; 8:793–803. DOI: 10.1016/j.nano.2011.11.003 [PubMed: 22100753]
55. Ohtsuki C, Kamitakahara M, Miyazaki T. Bioactive ceramic-based materials with designed reactivity for bone tissue regeneration. J R Soc Interface. 2009; 6(Suppl 3):S349–60. DOI: 10.1098/rsif.2008.0419.focus [PubMed: 19158015]
56. Hill R. An alternative view of the degradation of bioglass. J Mater Sci Lett. 1996; 15:1122–1125. DOI: 10.1007/BF00539955
57. Wong Po Foo C, Patwardhan SV, Belton DJ, Kitchel B, Anastasiades D, Huang J, Naik RR, Perry CC, Kaplan DL. Novel nanocomposites from spider silk-silica fusion (chimeric) proteins. Proc Natl Acad Sci U S A. 2006; 103:9428–33. DOI: 10.1073/pnas.0601096103 [PubMed: 16769898]
58. Mieszawska AJ, Nadkarni LD, Perry CC, Kaplan DL. Nanoscale control of silica particle formation via silk-silica fusion proteins for bone regeneration. Chem Mater. 2010; 22:5780–5785. DOI: 10.1021/cm101940u [PubMed: 20976116]
59. Plowright R, Dinjaski N, Zhou S, Belton DJ, Kaplan DL, Perry CC. Influence of silk–silica fusion protein design on silica condensation in vitro and cellular calcification. RSC Adv. 2016; 6:21776–21788. DOI: 10.1039/C6RA03706B [PubMed: 26989487]
60. Altman GH, Diaz F, Jakuba C, Calabro T, Horan RL, Chen J, Lu H, Richmond J, Kaplan DL. Silk-based biomaterials. Biomaterials. 2003; 24:401–16. [accessed November 7, 2016] http://www.ncbi.nlm.nih.gov/pubmed/12423595. [PubMed: 12423595]
61. Santin M, Motta A, Freddi G, Cannas M. In vitro evaluation of the inflammatory potential of the silk fibroin. J Biomed Mater Res. 1999; 46:382–9. [accessed November 7, 2016] http://www.ncbi.nlm.nih.gov/pubmed/10397996. [PubMed: 10397996]
62. Elia R, Guo J, Budijono S, Normand V, Benczédi D, Omenetto F, Kaplan DL. Encapsulation of Volatile Compounds in Silk Microparticles. J Coatings Technol Res. 2015; 12:793–799. DOI: 10.1007/s11998-015-9668-1
63. Meinel L, Hofmann S, Karageorgiou V, Kirker-Head C, McCool J, Gronowicz G, Zichner L, Langer R, Vunjak-Novakovic G, Kaplan DL. The inflammatory responses to silk films in vitro and in vivo. Biomaterials. 2005; 26:147–55. DOI: 10.1016/j.biomaterials.2004.02.047 [PubMed: 15207461]
64. Panilaitis B, Altman GH, Chen J, Jin HJ, Karageorgiou V, Kaplan DL. Macrophage responses to silk. Biomaterials. 2003; 24:3079–85. [accessed November 7, 2016] http://www.ncbi.nlm.nih.gov/pubmed/12895580. [PubMed: 12895580]
65. Canabady-Rochelle LLS, Belton DJ, Deschaume O, Currie HA, Kaplan DL, Perry CC. Bioinspired silicification of silica-binding peptide-silk protein chimeras: comparison of chemically and genetically produced proteins. Biomacromolecules. 2012; 13:683–90. DOI: 10.1021/bm201555c [PubMed: 22229696]
66. Lechner CC, Becker CFW. A sequence-function analysis of the silica precipitating silaffin R5 peptide. J Pept Sci. 2014; 20:152–158. DOI: 10.1002/psc.2577 [PubMed: 25975421]

67. Dinjaski N, Ebrahimi D, Ling S, Shah S, Buehler MJ, Kaplan DL. Integrated Modeling and Experimental Approaches to Control Silica Modification of Design Silk-Based Biomaterials. ACS Biomater Sci Eng. 2016; acsbiomaterials.6b00236. doi: 10.1021/acsbiomaterials.6b00236

68. Plowright R, Dinjaski N, Zhou S, Belton DJ, Kaplan DL, Perry CC. Influence of silk–silica fusion protein design on silica condensation in vitro and cellular calcification. RSC Adv. 2016; 6:21776–21788. DOI: 10.1039/C6RA03706B [PubMed: 26989487]

69. Wang X, Schröder HC, Wiens M, Ushijima H, Müller WEG. Bio-silica and bio-polyphosphate: applications in biomedicine (bone formation). Curr Opin Biotechnol. 2012; 23:570–8. DOI: 10.1016/j.copbio.2012.01.018 [PubMed: 22366413]

70. Izadifar Z, Chen X, Kulyk W. Strategic design and fabrication of engineered scaffolds for articular cartilage repair. J Funct Biomater. 2012; 3:799–838. DOI: 10.3390/jfb3040799 [PubMed: 24955748]

71. O'Shea TM, Miao X. Bilayered scaffolds for osteochondral tissue engineering. Tissue Eng Part B Rev. 2008; 14:447–64. DOI: 10.1089/ten.teb.2008.0327 [PubMed: 18844605]

72. Glimcher MJ. Mechanism of calcification: role of collagen fibrils and collagen-phosphoprotein complexes in vitro and in vivo. Anat Rec. 1989; 224:139–53. DOI: 10.1002/ar.1092240205 [PubMed: 2672881]

73. Marner WD, Shaikh AS, Muller SJ, Keasling JD. Morphology of artificial silica matrices formed via autosilification of a silaffin/protein polymer chimera. Biomacromolecules. 2008; 9:1–5. DOI: 10.1021/bm701131x [PubMed: 18092760]

74. Wiens M, Wang X, Schlossmacher U, Lieberwirth I, Glasser G, Ushijima H, Schröder HC, Müller WEG. Osteogenic potential of biosilica on human osteoblast-like (SaOS-2) cells. Calcif Tissue Int. 2010; 87:513–24. DOI: 10.1007/s00223-010-9408-6 [PubMed: 20725824]

75. Barragan-Adjemian C, Nicolella D, Dusevich V, Dallas MR, Eick JD, Bonewald LF. Mechanism by which MLO-A5 late osteoblasts/early osteocytes mineralize in culture: similarities with mineralization of lamellar bone. Calcif Tissue Int. 2006; 79:340–53. DOI: 10.1007/s00223-006-0107-2 [PubMed: 17115241]

76. Landis WJ. An overview of vertebrate mineralization with emphasis on collagen-mineral interaction. Gravit Space Biol Bull. 1999; 12:15–26. [accessed November 7, 2016] http://www.ncbi.nlm.nih.gov/pubmed/11541779. [PubMed: 11541779]

77. Correia C, Bhumiratana S, Yan LP, Oliveira AL, Gimble JM, Rockwood D, Kaplan DL, Sousa RA, Reis RL, Vunjak-Novakovic G. Development of silk-based scaffolds for tissue engineering of bone from human adipose-derived stem cells. Acta Biomater. 2012; 8:2483–92. DOI: 10.1016/j.actbio.2012.03.019 [PubMed: 22421311]

78. Eggli PS, Hunziker EB, Schenk RK. Quantitation of structural features characterizing weight- and less-weight-bearing regions in articular cartilage: a stereological analysis of medial femoral condyles in young adult rabbits. Anat Rec. 1988; 222:217–27. DOI: 10.1002/ar.1092220302 [PubMed: 3213972]

79. Swann AC, Seedhom BB. The stiffness of normal articular cartilage and the predominant acting stress levels: implications for the aetiology of osteoarthrosis. Br J Rheumatol. 1993; 32:16–25. [accessed November 7, 2016] http://www.ncbi.nlm.nih.gov/pubmed/8422553. [PubMed: 8422553]

80. Benjamin M, Evans EJ, Copp L. The histology of tendon attachments to bone in man. J Anat. 1986; 149:89–100. [PubMed: 3693113]

81. Cooper RR, Misol S. Tendon and ligament insertion. A light and electron microscopic study. J Bone Joint Surg Am. 1970; 52:1–20. http://www.ncbi.nlm.nih.gov/pubmed/4189231. [PubMed: 4189231]

82. Lu HH, Subramony SD, Boushell MK, Zhang X. Tissue Engineering Strategies for the Regeneration of Orthopedic Interfaces. Ann Biomed Eng. 2010; 38:2142–2154. DOI: 10.1007/s10439-010-0046-y [PubMed: 20422291]

83. Moffat KL, Wang INE, Rodeo SA, Lu HH. Orthopedic Interface Tissue Engineering for the Biological Fixation of Soft Tissue Grafts. Clin Sports Med. 2009; 28:157–176. DOI: 10.1016/j.csm.2008.08.006 [PubMed: 19064172]

84. Altman GH, Horan RL, Lu HH, Moreau J, Martin I, Richmond JC, Kaplan DL. Silk matrix for tissue engineered anterior cruciate ligaments. Biomaterials. 2002; 23:4131–4141. DOI: 10.1016/S0142-9612(02)00156-4 [PubMed: 12182315]
85. Kim U-J, Park J, Joo Kim H, Wada M, Kaplan DL. Three-dimensional aqueous-derived biomaterial scaffolds from silk fibroin. Biomaterials. 2005; 26:2775–2785. DOI: 10.1016/j.biomaterials.2004.07.044 [PubMed: 15585282]
86. Wang Y, Rudym DD, Walsh A, Abrahamsen L, Kim HJ, Kim HS, Kirker-Head C, Kaplan DL. In vivo degradation of three-dimensional silk fibroin scaffolds. Biomaterials. 2008; 29:3415–3428. DOI: 10.1016/j.biomaterials.2008.05.002 [PubMed: 18502501]
87. Wang Y, Kim HJ, Vunjak-Novakovic G, Kaplan DL. Stem cell-based tissue engineering with silk biomaterials. Biomaterials. 2006; 27:6064–82. DOI: 10.1016/j.biomaterials.2006.07.008 [PubMed: 16890988]
88. Gibson, LJ., Ashby, MF. Cellular Solids — Structure and Properties. Cambridge University Press; Cambridge: 1997.
89. Otzen D. The Role of Proteins in Biosilicification. Scientifica (Cairo). 2012; 2012:1–22. DOI: 10.6064/2012/867562
90. Rodríguez F, Glawe DD, Naik RR, Hallinan KP, Stone MO. Study of the Chemical and Physical Influences upon in Vitro Peptide-Mediated Silica Formation. Biomacromolecules. 2004; 5:261–265. DOI: 10.1021/bm034232c [PubMed: 15002982]

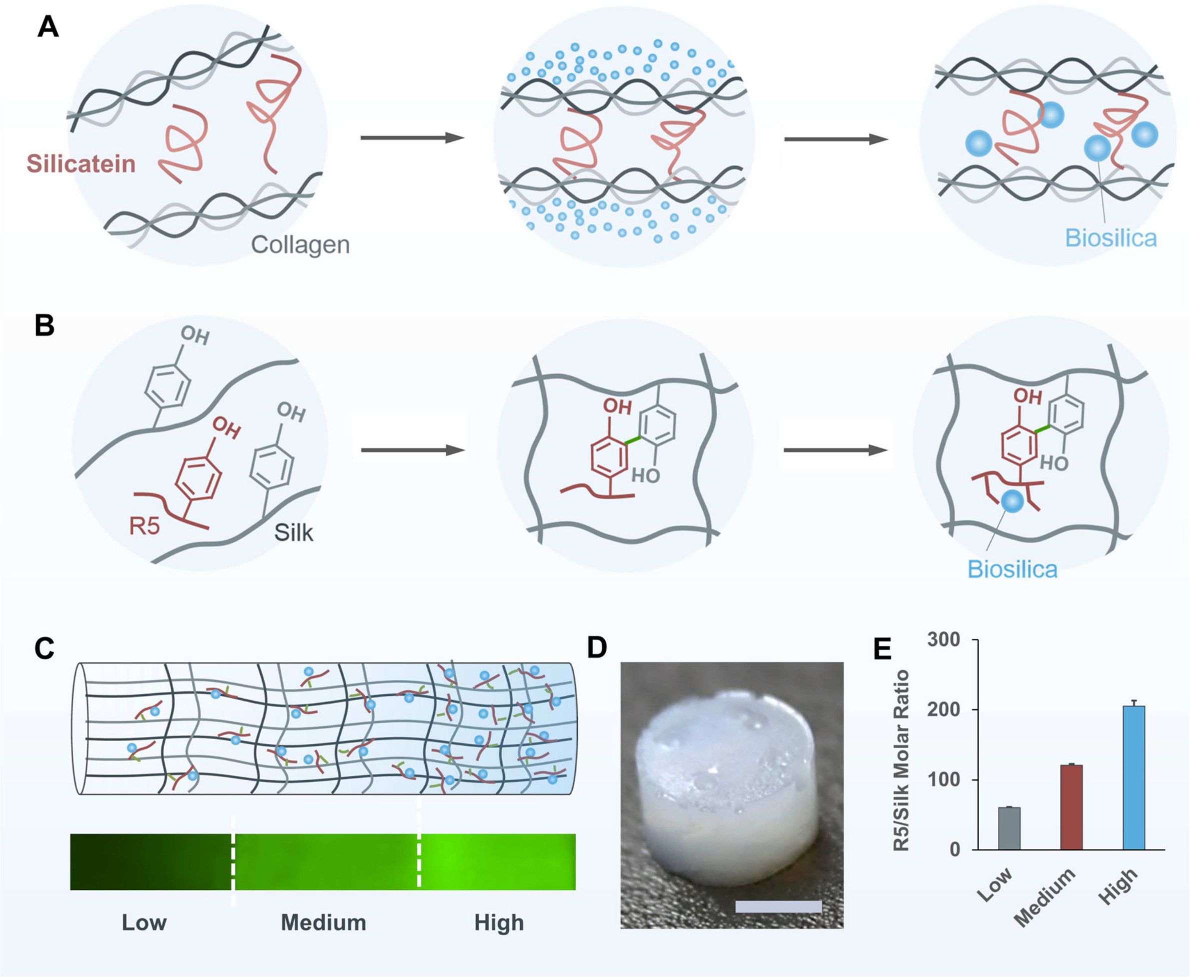

Figure 1.

Biomimetic design of the GSSR5 composites. Silicatein mediates the formation of biosilica particles within the siliceous spicules which is organized by collagen in sponge (A). Biomimetic self-assembly of biosilica particles on the silk templates catalyzed by the biosilica selective peptide R5 (B). Schematic representation of the biomimetic GSSR5 composites and fluorescence microscopy image showing the gradient of FITC-labeled R5 peptide along the longitudinal direction of the composites (C). The high region contains a high content of the R5 peptide and biosilica particles in contrast to the transition to the medium and low regions where the contents diminish. Gross appearance of the GSSR5 composites (D). Molar ratio of R5/silk in the GSSR5 composites (E), showing gradually increasing concentration of the R5 peptide from the low to the high R5 peptide loading regions in the gradient composites. Scale bar, 2 mm.

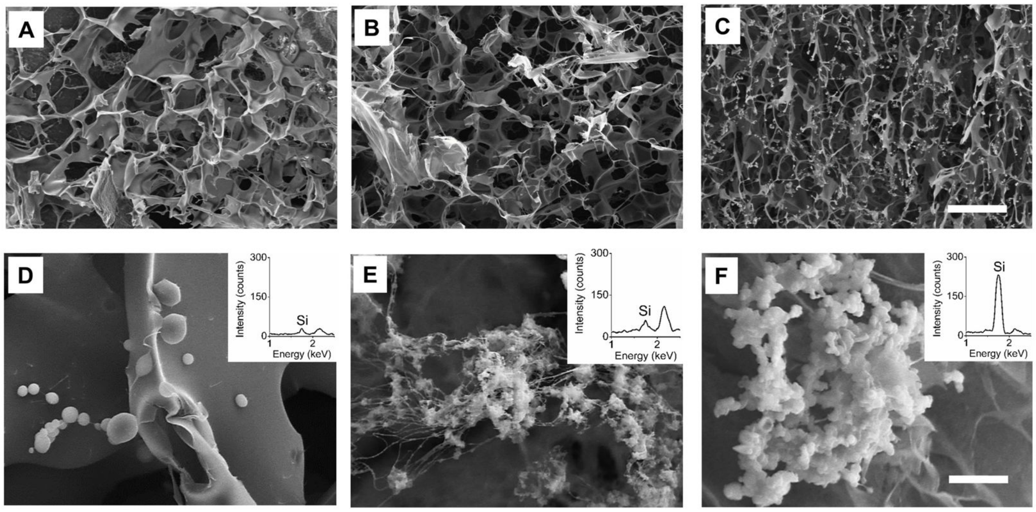

Figure 2.

SEM images of the GSSR5 composites with low (A, D), medium (B, E) and high (C, F) loadings of the R5 peptide, respectively. EDS spectra (the inserted images) of the GSSR5 composites with low (D), medium (E) and high (F) loading of the R5 peptide. Scale bars are 50 μm (top), 5 μm (bottom). SEM, scanning electron microscopy; EDS, energy-dispersive X-ray spectroscopy. The final GSSR5 composites exhibited uniform porous structure in three regions, while the pore sizes gradually decreased from the low region to the high region in the GSSR5 composites. The increasing distribution of biosilica particles was observed from low to high regions in the composites, which was further confirmed by EDS tests.

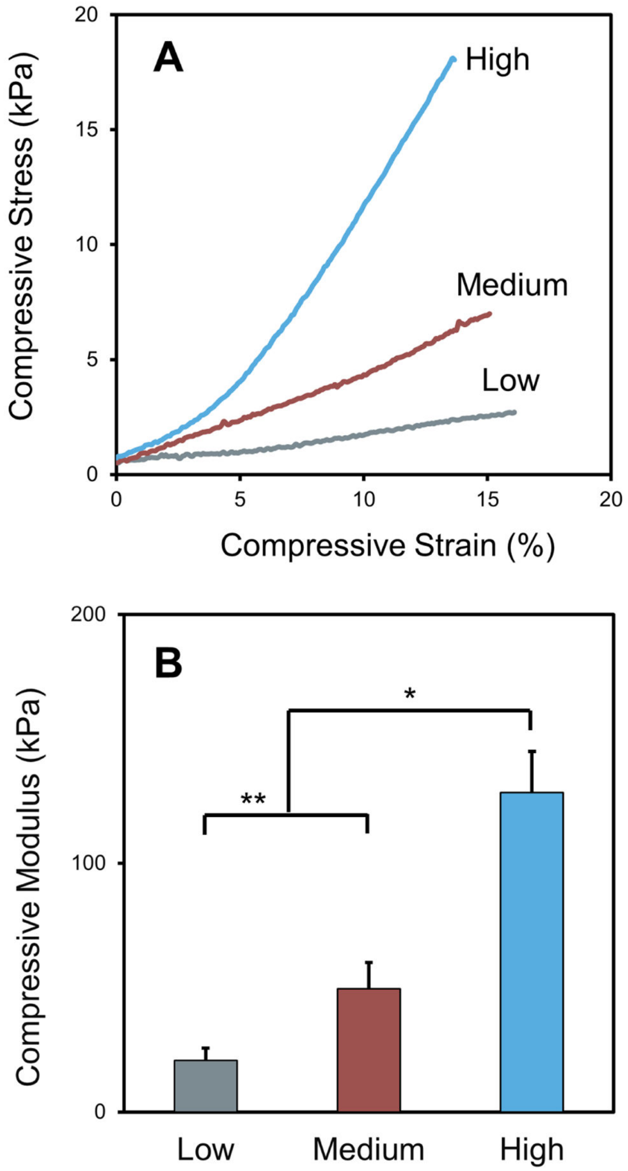

Figure 3.

Representative stress-strain curves (A) and compressive moduli (B) of the low, medium and high regions in the GSSR5 composites. An approximately 6-fold increase in the compressive Young's modulus from low to high regions were achieved in the GSSR5 composites. (*$p < 0.01$, **$p<0.05$)

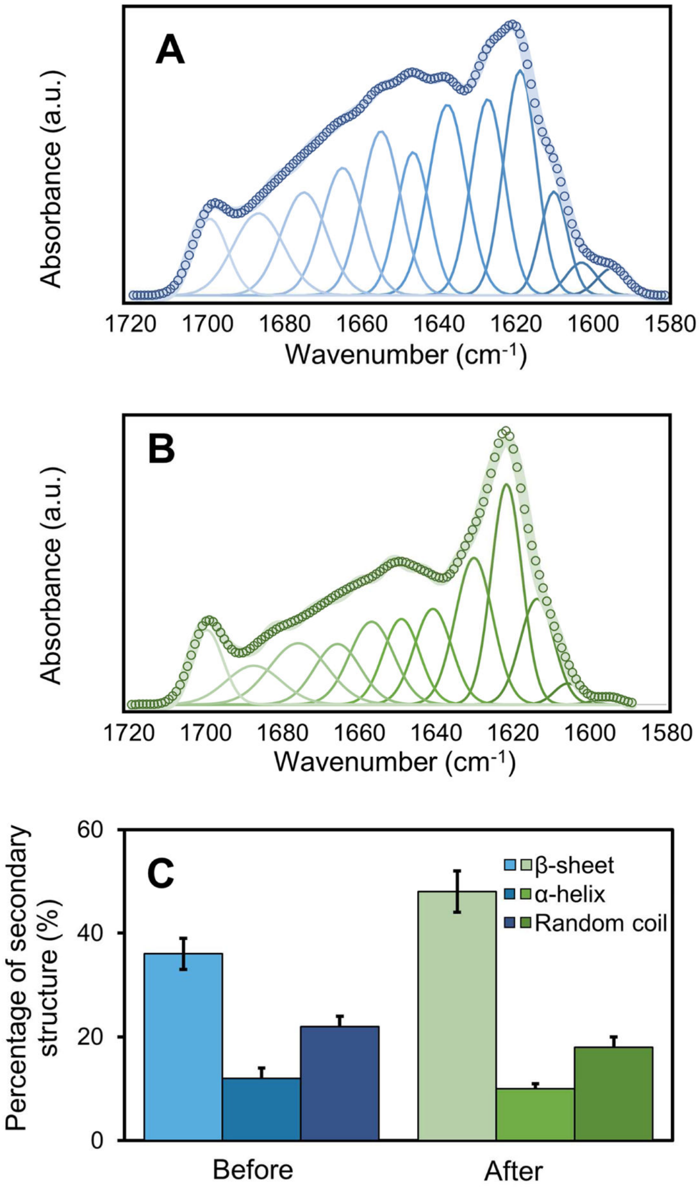

Figure 4.

Representative Fourier self-deconvolution of amide I spectra for the silk/R5 composite before (A) and after (B) silicification. Percentage of the secondary structural elements in the composites (C). Key: open circles, measured data; wide solid line, summation of Gaussian peaks; thin solid lines, individual amorphous Gaussian peaks. The assignment of amide I bands was taken from the literature [38,40]. The content of non-crystalline structures including random coil and α-helix simultaneously diminished after silicification (α-helix: from 12±2% to 10±1%; random coil: from 22±2% to 18±2%), while the percentage of β-sheet crystalline structure increased after silicification (from 36±3% to 48±4%).

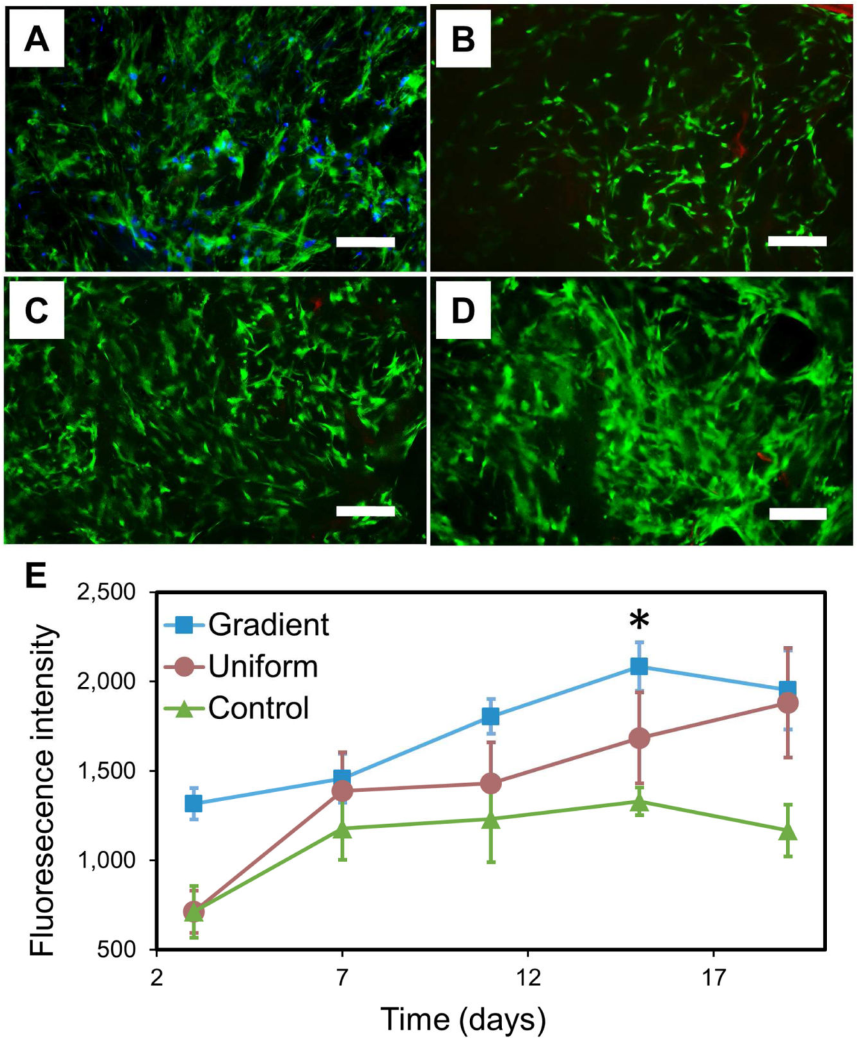

Figure 5.

Fluorescence staining of actin (green) and nuclei (blue) of hMSCs in the GSSR5 composites in growth medium at day 19 (A). HMSCs spread out actin filaments, aligned with the pores and evenly distributed in the GSSR5 composites after 19-day culture. Live/dead staining of hMSCs cultured in the GSSR5 composites in growth medium at day 3 (B), day 11 (C) and day 19 (D). Strong green fluorescence with minimal visible red fluorescence demonstrated the cytocompatibility of the material. Alamar blue assay (E) showed the proliferation of hMSCs in the gradient (square), uniform (circle) and unsilicified plain silk control (triangular) composites over a 19-day period (n>3). Uniform silicified silk/R5 composites had a silk/R5 molar ratio of 1/125. Unsilicified plain silk composites served as controls. Scale bar, 200 μm. (*Significantly different from day 3 ($p < 0.01$))

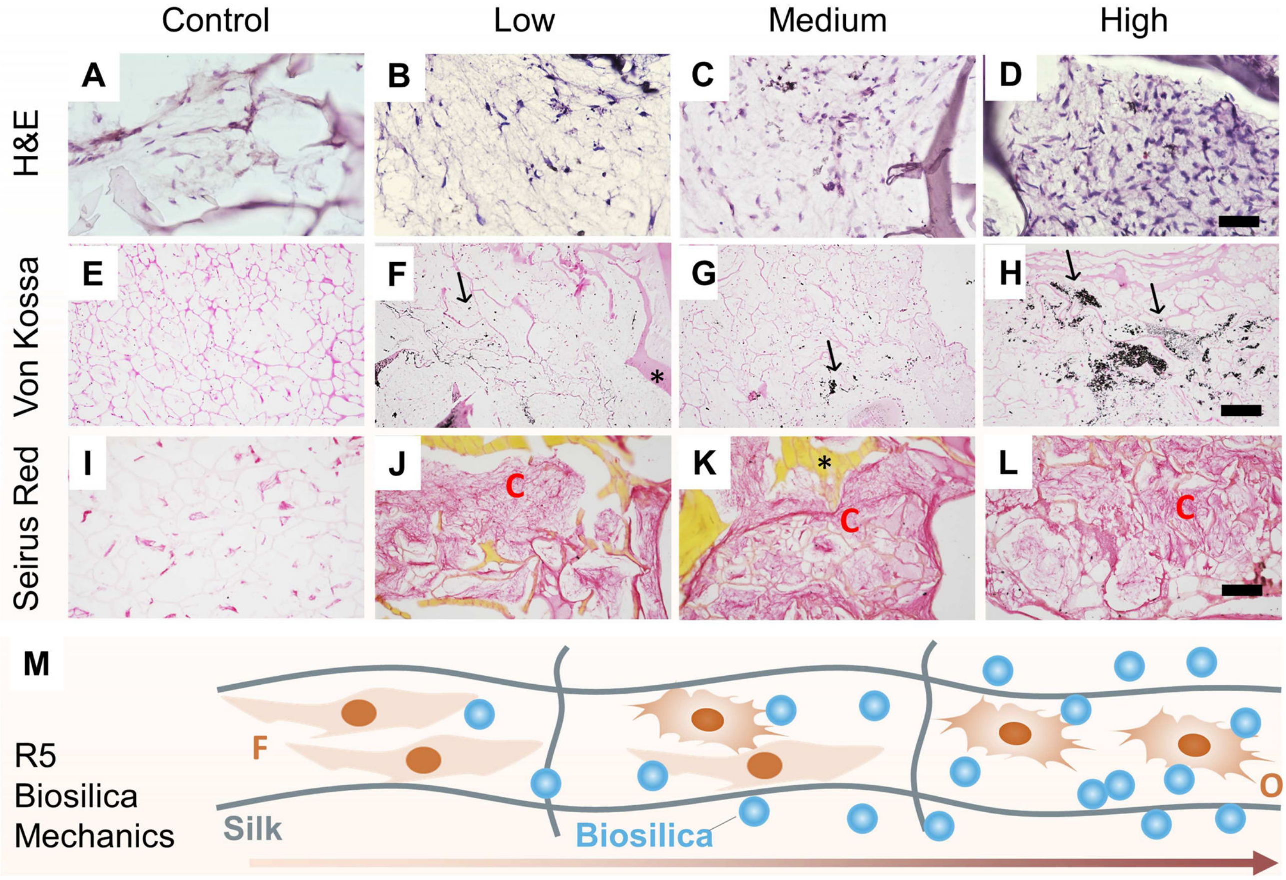

Figure 6.

Histological sections taken from the unsilicified plain silk controls (A, E, I), and the GSSR5 composites with low (B, F, J), medium (C, G, K) and high (D, H, L) loadings of the R5 peptide after 6-week culture of hMSCs in osteogenic medium. H&E staining (A, B, C, D), von Kossa staining (E, F, G, H) and Sirius red staining (I, J, K, L). Schematic representation of cell differentiation along the GSSR5 composites (M). Scale bar, 50 μm (A–D); 200 μm (E–L). Unsilicified plain silk composites served as controls. Arrows indicate calcification; asterisks indicate composites. O, osteoblast-like cells; C, collagen-like bundles; F, fibroblast-like cells.

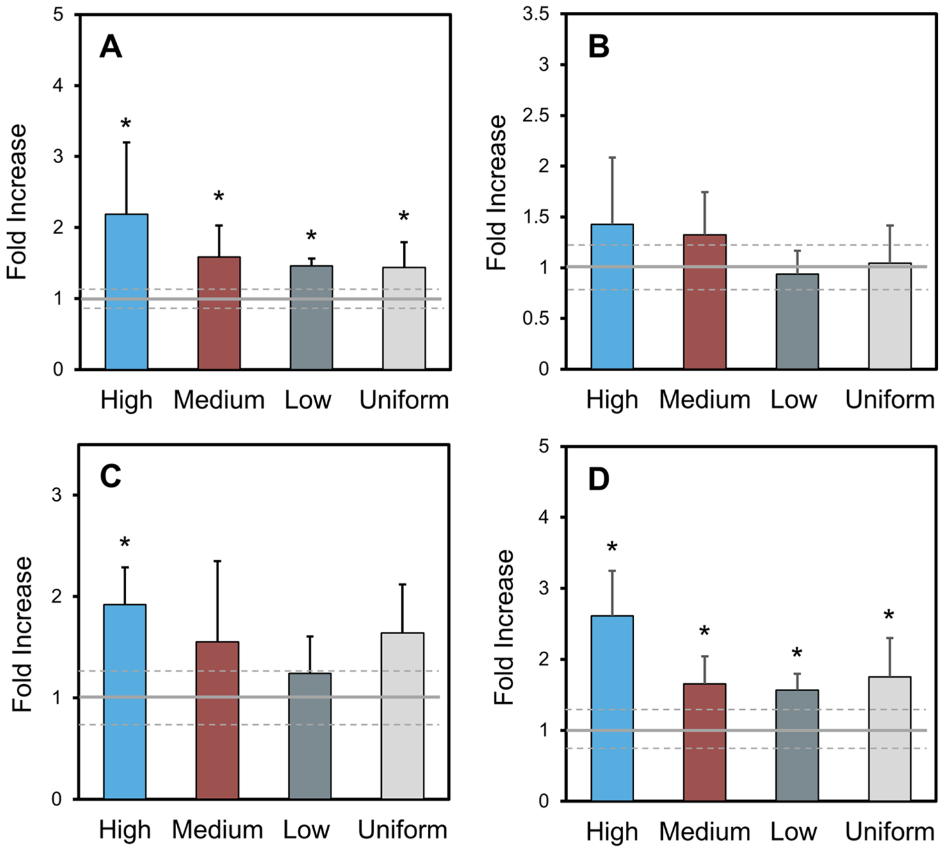

Figure 7.

Transcript levels from hMSCs cultured in the GSSR5 composites under osteogenic conditions after 6 weeks. Expression of Runx2 (A), collagen type I (B), alkaline phosphatase (ALP, C) and bone sialoprotein (BSP, D). Data are shown relative to the expression of the respective genes in hMSCs cultured in unsilicified plain silk controls. Uniform silicified silk/R5 composites had a silk to R5 molar ratio of 1 to 125. The solid grey line represents the average of control and standard deviation is represented by dashed grey line. (*Significantly different from unsilicified silk controls ($p < 0.05$))

Table 1

Quantification of the R5 peptide in the GSSR5 composites using FITC labeling technique.

R5 loading	**Low**	**Medium**	**High**
Silk/R5 synthesis ratio[a]	1/62.5	1/125	1/250
R5 released (%)[b]	3.8±2.0	3.2±1.4	7.9±3.3
Silk/R5 final ratio[c]	1/60	1/121	1/205
Encapsulation efficiency (%)[d]	96.2±2.0	96.8±1.4	92.1±3.3

[a] Silk/R5 molar ratio in the GSSR5 composites, determined by the amount of silk and R5 loaded to the composites.

[b] The release of the R5 peptide through the process of silicification, determined by

[c] quantifying the amount of the FITC-R5 peptide released to the silicifying media. Silk/R5 molar ratio after silicification.

[d] Encapsulation efficiencies of the GSSR5 composites